How to cite: *Angew. Chem. Int. Ed.* **2023,** *62,* e202304303
doi.org/10.1002/anie.202304303

MOF for Heterogeneous Catalysis

Kinetic Control via Binding Sites within the Confined Space of Metal Metalloporphyrin-Frameworks for Enhanced Shape-Selectivity Catalysis

*Weijie Zhang[+], Zhou Lu[+], Lukasz Wojtas, Yu-Sheng Chen, Alexander A. Baker, Yi-Sheng Liu, Abdullah M. Al-Enizi, Ayman Nafady, and Shengqian Ma**

Abstract: One striking feature of enzyme is its controllable ability to trap substrates via synergistic or cooperative binding in the enzymatic pocket, which renders the shape-selectivity of product by the confined spatial environment. The success of shape-selective catalysis relies on the ability of enzyme to tune the thermodynamics and kinetics for chemical reactions. In emulation of enzyme's ability, we showcase herein a targeting strategy with the substrate being anchored on the internal pore wall of metal-organic frameworks (MOFs), taking full advantage of the sterically kinetic control to achieve shape-selectivity for the reactions. For this purpose, a series of binding site-accessible metal metalloporphyrin-frameworks (MMPFs) have been investigated to shed light on the nature of enzyme-mimic catalysis. They exhibit a different density of binding sites that are well arranged into the nanospace with corresponding distances of opposite binding sites. Such a structural specificity results in a facile switch in selectivity from an exclusive formation of the thermodynamically stable product to the kinetic product. Thus, the proposed targeting strategy, based on the combination of porous materials and binding events, paves a new way to develop highly efficient heterogeneous catalysts for shifting selectivity.

Introduction

The importance of shape-selectivity in zeolite catalysis has been well-recognized in the petroleum and chemical industries.[1] Strong correlations have been observed between the catalytic shape-selectivity and the nanoporous environment. For example, upon encapsulation by zeolite crystals, the selectivity of the metal catalyst can be improved since small pores hinder the access of large-sized bulky substrate to the metal surface, which is known as size-selectivity; meanwhile, the small pores can inhibit the formation and diffusion of product with suitable dimension and shape to achieve shape-selectivity.[2] Generally, for porous materials, shape-selectivity occurs when, among the isomeric reaction intermediates formed within a crowded space, only those with the proper orientations can appear as major products.

Enzymes have exquisite selectivity, capable of choosing a single substrate from compounds with a similar structure.[3] The tertiary protein structures of enzymes suggest that the molecular-sized substrate binding sites offer them a strong ability to control the transition between thermodynamics and kinetics. Their shape-selectivity arises from the difference between the absolute activation barriers of the thermodynamic or kinetic pathway; that is, the variation in absolute barrier heights determines the selectivity. Similarly, zeolites with a rigid framework have internal voids of molecular dimensions. Albeit zeolite mimics of enzyme functions have been well developed,[4] it remains challenging to design a porous material to strike a balance between thermodynamic and kinetic control.

Over the past decade, considerable efforts have been devoted to developing metal-organic framework (MOF) structures that mimic the enzyme pockets.[5] Various types of interactions inside pockets have been investigated to highlight the nature of analogous enzymatic catalysis as well as to develop highly efficient and specific synthetic catalysts.[6] For instance, some non-covalent interactions, such as van der Waals forces,[7] hydrogen bonding interactions,[8] π···π interactions[9] and halogen bonding interactions,[10] can modulate the activity inside the micropores for catalytic

[*] W. Zhang,[+] Z. Lu,[+] S. Ma
Department of Chemistry, University of North Texas
Denton, TX-76203 (USA)
E-mail: Shengqian.Ma@unt.edu

L. Wojtas
Department of Chemistry, University of South Florida
Tampa, FL-33620 (USA)

Y.-S. Chen
ChemMatCARS, Center for Advanced Radiation Sources, The University of Chicago
Argonne, IL-60439 (USA)

A. A. Baker
Lawrence Livermore National Laboratory
Livermore, CA-94550 (USA)

Y.-S. Liu
Advanced Light Source, Lawrence Berkeley National Laboratory
Berkeley, CA-94720 (USA)

A. M. Al-Enizi, A. Nafady
Department of Chemistry, College of Science, King Saud University
Riyadh 11451 (Saudi Arabia)

[+] These authors contributed equally to this work.

transformations. Recently, coordination-based control has led to the rapid growth of applications in MOF catalysis.[11] This is mainly because the unsaturated metal site can moderately coordinate with a substrate to stabilize the negative charge in the transition state, enhance the mass diffusion, and reassemble the starting material close enough for the catalysis reaction.[12] In this work, we demonstrated an efficient strategy to enhance shape-selectivity by coupling coordination-driven binding and steric hindrance controlled by pore size.

There are significant differences among the surface catalysis, catalysis in the pockets without binding sites and catalysis in the binding pockets, when the geometries of thermodynamic product and kinetic product differ from each other (kinetic product C_1 and thermodynamic product C_2 in Figure 1a–d). When the surface catalysis (route 1), or catalysis in the pockets without binding sites (route 2) or catalysis in the binding pockets without steric control (route 3) occurs, it is difficult to precisely control the shape-selectivity, especially for the targeted synthesis of kinetic product (C_1). The thermodynamically more stable product C_2 dominates in the final products associated with the lowest energy barrier. Inspired by the investigations on the steric-control selectivity assisted by the favorable geometry,[13] we hypothesize that, if the substrate can be "anchored" on the internal wall instead of loosely residing in the pocket, the pore size will only facilitate the formation of products with a particular shape (Figure 1d); in such way, the thermodynamic control and kinetic control can be reversed via changing the energy barrier (Figure 1e). Such kind of kinetic control for high shape-selectivity in heterogeneous systems can be targeted via creating binding pockets with coordination "anchoring" sites within highly porous MOFs, as proposed herein.

In this contribution, a family of metal-metalloporphyrin frameworks (MMPF-2,[14] MMPF-3,[10,15] MMPF-5[16] and MMPF-11) featuring catalytic binding pockets are employed for proof-of-concept studies to illustrate the kinetic control for shape-selectivity. The results showed that MMPF-11 with appropriate binding pocket size exhibited a high shape-selectivity and made the Hantzsch reaction produce the corresponding 1,4-dihydropyridines (1,4-DHPs) as the main product under mild conditions, which, to the best of our knowledge, represents the first mutually combining the thermodynamic control from binding and kinetic control from the confined pocket to promote shape-selectivity in a heterogeneous manner.

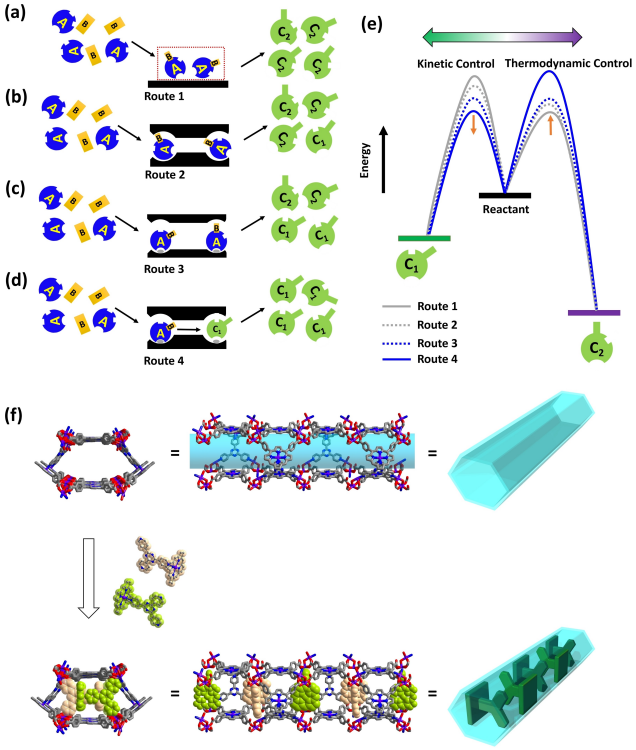

Figure 1. a)–e) Four mechanistic examples of size-dependent shape-specificity in the reactions, on the surfaces dominated by the thermodynamic control (Route 1), inside the pockets without binding events (Route 2), inside the binding pockets without confined space (Route 3) or inside the binding pockets fully controlled by the steric kinetic (Route 4). f) The detailed crystal structure of MMPF-11 including the view of the 1D hexagonal channel in MMPF-11 and 1D hexagonal channel locked by a composition of $\mathbf{L_1}$-Co-TCPP ligand stacking in parallel that is anchored to channel wall on Co dimer cluster. $\mathbf{L_1}$ = 2,4,6-*tri*(4-pyridinyl)-1,3,5-triazine.

Results and Discussion

One way to create a binding pocket with controlled size in MOF can turn to the insertion of judiciously selected pillar ligands[17] and the coordination "anchoring" sites can be built on the pore walls by the employment of metal-loporphyrins as backbones, of which the metal ions within the porphyrin macrocyles can recognize certain substrates like some metalloenzymes. Bearing these in mind, we selected the functionalized triangle pillar ($\mathbf{L_1}$ = 2,4,6-*tri*(4-pyridinyl)-1,3,5-triazine) instead of the traditional linear pillar for insertion into MMPF to control the binding pocket size. Solvothermal reaction of meso-tetrakis(4-carboxyphenyl)porphyrin (TCPP), **L1** and $Co(NO_3)_2$ in N,N-dimethylformamide (DMF) at 100 °C for 72 h in sealed vials afforded rod-shaped purple crystals of MMPF-11 with the empirical formula of $[Co_4O_4(DMF)_2](Co\text{-}TCPP)_3(\mathbf{L1})_2\cdot(H_2O)_n$, as determined by X-ray crystallography,[18] elemental analyses, and thermogravimetric analysis (Figure S1).

Single-crystal X-ray diffraction studies revealed that MMPF-11 crystallizes in the space group *Pbcm*. MMPF-11 possesses readily accessible Co metal sites and features permit-required confined cavities. As shown in Figure 1f, the hexagonal channel in MMPF-11 consists of two Co dimer clusters (Figure S2) linked by the square planar TCPP ligands and triangular **L1** pillars. The two-component assembled unit ($\mathbf{L_1}$-Co-TCPP) as bolt locks the 1D hexagonal channel of MMPF-11 into separate pockets, thus resulting in an open cavity at distances of 1.6 nm (Figure S3). Non-interpenetrated structure for MMPF-11 is important for shape-selective recognition, due to the need for large cavities and opening sites to allow the anchoring of reactants into designed pocket environments. Our attempts to bridge

the linear pillars (pyrazine or 4,4'-bipyridine) with the 2D porphyrin layers via coordinating the Co metal centers within the paddlewheels did not afford MMPFs with accessible metal centers.

The purity of bulk MMPF-11 sample was confirmed via powder X-ray diffraction (PXRD) analysis (Figure S4), the patterns of which matched well those calculated from the CIF file. ICP-MS confirmed the proposed metal ratios. The as-synthesized MMPF-11 has approximately two **L1** pillar attached to Co-TCPP, as quantified by the ^{1}H NMR spectrum (Figure S5). Thermogravimetric analysis (TGA) of MMPF-11 (Figure S6) showed a weight loss of 18 % between 50 and 241 °C, corresponding to the loss of H_2O, ethanol and DMF molecules. Additionally, TGA traces of MMPF-11 crystals after being activated with supercritical CO_2 fluid did not show significant weight loss up to 420 °C, indicating that the pores have been fully evacuated while the frameworks are thermally stable. Furthermore, the permanent porosity of MMPF-11 was confirmed by CO_2 adsorption at 273 K, which revealed a BET surface area of 590 $m^2 g^{-1}$ (Figure S7).[19]

In recent years, much attention has been paid to the synthesis of 1,4-DHPs due to their relevant biological activity.[20] As shown in Figure 2a, the mechanism is the nucleophilic addition of -NH_2 to an α,β-unsaturated carbonyl compound. However, it remains challenging to achieve a high shape-selectivity and make the Hantzsch reaction produce the corresponding 1,4-DHPs as the main product under mild conditions.[21] This is because the reaction proceeds via 1,4 addition and it is difficult to produce 1,4-DHPs at room temperature. For the first stage, the reaction occurs via a condensation of the 1,3-dicarbonyl compound with the aldehyde to yield an α,β-unsaturated carbonyl molecule (substrate A, as mentioned in Figure 2a) and a condensation of ammonia with another equivalent of the 1,3-dicarbonyl compound to produce an enamine (substrate B, as mentioned in Figure 2a). Therefore, the product, 1,4-DHP (C_1) or 1,2-DHP (C_2) depends on the enamine intermediate which favors to attack the carbon atom of the C=O double bond (C1 in Figure 2a) or the carbon atom of the C=C double bond (C_2 in Figure 2a).

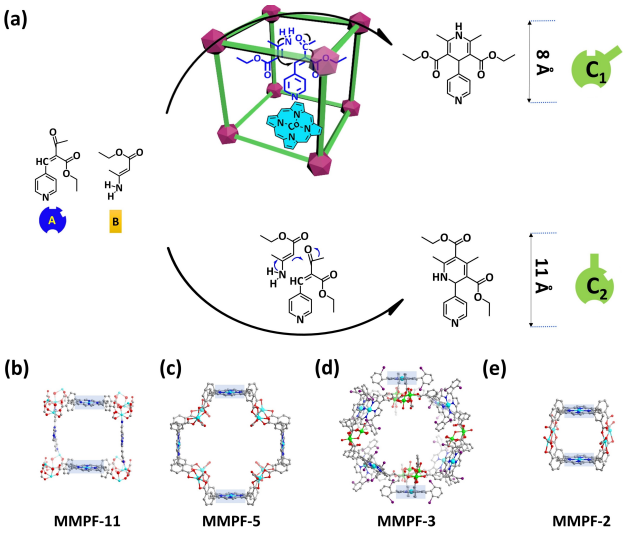

Figure 2. a) The proposed mechanisms for the synthesis of 1,4-DHP (C1) via the targeting strategy compared to the formation of 2-aryl-pyridine (C2). b)–e) The crystal structures of MMPF-11, MMPF-5, MMPF-3 and MMPF-2.

Considering that MMPF-11 (Figure 2b) has Co-metalated porphyrin units in nanospace which are capable of reversible binding and releasing of the guest molecules, its catalytic activity was first examined for the Hantzsch reaction. When α,β-unsaturated carbonyl (Substrate A, 1 mmol) and enamine (Substrate B, 1 mmol) were added to THF in the presence of MMPF-11 (1 mol %) at room temperature and 1 bar, the conversion was >99 % after 24 h, as estimated from GC-MS analysis. By contrast, only 30 % conversion was observed under the same reaction conditions in the presence of Co-TPP, which was comparable to the blank control reaction (i.e. without any catalyst) with a conversion of 21 %. Some other control experiments were conducted for MMPF-5 (Figure 2c), MMPF-3 (Figure 2d) and MMPF-2 (Figure 2e) under the same conditions (Scheme S1–S2 and Figure S8–S18, see the Supporting Information for details). MMPF-11, MMPF-5 and MMPF-3 were more active than the others for the Hantzsch reaction. Given their structural specificity, we ascribed the higher catalytic activity of MMPF-11, MMPF-5 and MMPF-3 in comparison with other controls mainly to the high density of binding sites from Co-porphyrin moieties that are well arranged into the nanospace.

Based upon the abovementioned results, another control experiment was carried out using a similar substrate, in which the pyridine moiety was replaced with benzene (Table S1 and Figure S19). The replacement of pyridine with benzene led to a significant drop in the rate of the reaction, with both reactions only reaching 14 % conversion after 24 h and product ratio of 36:64. This roughly confirmed our proposed targeting strategy that the catalysis requires substrate to bind to the host MMPF-11 with a high DFT-calculated binding energy of −58.9 kcal mol^{-1} (Table S2). During the control experiments, the reaction rate for 4-pyridinecarboxaldehyde conversion is faster than that of the enone conversion and 1,4-DHPs yield (Figure S20). As previously proposed from NMR measurements,[22] the enamine and enone intermediate indeed participate in the rate-limiting step (Figure S21). Moreover, MMPF-11 showed good recyclability for more than four catalytic cycles, giving conversion over 95 % and shape-selectivity 79 % under the same conditions. The consistent PXRD patterns of the recovered and freshly prepared samples of MMPF-11 suggested the structural integrity of the catalyst after the catalytic cycle (Figure S2). For the PXRD after catalysis, there were some decreases in peak intensity compared to the as-synthesized pattern. This is because, after catalysis, bulky MMPF-11 crystals were fractured into tiny crystals after mechanical stirring. We also observed several missing peaks in XRD, which could be presumably due to the distortion of crystalline structure at least in some specific directions.[23]

It is worth noting that the distance between the Co-anchoring sites of two opposite porphyrin walls in MMPF-11 is around 1.6 nm and such distance is more favorable for a shorter isomeric reaction intermediate to allow the effective formation of 1,4-DHPs (product C_1). Therefore, MMPF-11 afforded the products C_1 and C_2 in a high ratio of 85:15, indicating that the pocket imposes geometric constraints to guide synthetic paths with predictable three-dimensional shape, as a kinetic control. Figure 2b–d showed the different pairings of Co-TCPP sites in MMPF-11, MMPF-5, MMPF-3, and MMPF-2 with their corresponding opposite Co–Co distances in Table 1. Reasoning that Co–Co distance must be sufficiently close to assist the formation of the enamine intermediate in the way illustrated in Figure 2a, we can figure out the cavities that could not possibly afford the kinetic target-guided synthesis of C_1. Given that van der Waals forces as the weakest intermolecular forces account for distances of less than 0.6 nm, the Co–Co distance of MMPF-11 (16 Å) is still seemingly close enough to facilitate the transformation of C_1 and suppress the production of C_2, thus demonstrating the highest shape selectivity (85 %).

Table 1: Conversion and product ratio of the Hantzsch reaction catalyzed by different catalysts.

Entry	Catalyst	Co–Co distance [Å]	Conversion [%]	Ratio (C_1:C_2)
1	MMPF-11	16	>99	85:15
2	Co-TPP	–	30	17:83
3	None	–	21	19:81
4	MMPF-5	22	>99	46:54
5	MMPF-3	29	>99	42:58
6	MMPF-2	10	42	20:80

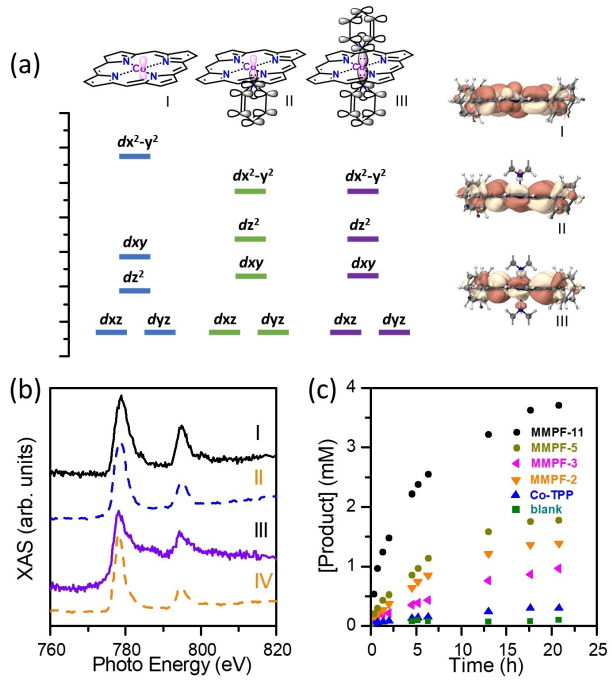

Figure 3. a) The energy orderings of Co 3*d* orbitals in (I) square planar four-, (II) square pyramidal five-, and (III) octahedral six-coordination modes. Inset: HOMO contours of Co-porphyrin I, II, and III with isovalues of 0.02 a.u. b) EY-XAS (solid line 5 nm) and FY-XAS (dashed line 100 nm) of MMPF-11 (I and II) and Co standard (III and IV) obtained in the Co L-edge region. Both spectra were obtained under normal ultra-high vacuum conditions. c) Progress curves for acyl transfer. The reaction was monitored by GC.

Theoretical calculations based on the structures of Co-porphyrins (I, II, and III in Figure 3a) were performed to investigate the 3*d* orbital splitting situation of Co sites. Notably, DFT results indicated that the axial coordination leads to the decline of $d_{x^2-y^2}$ and d_{xy} orbitals as well as simultaneous elevation of d_{z^2} orbitals. The strong interaction between axial pyridine and Co sites displaces the Co out of the porphyrin plane and results in decrease of anti-bonding characters with nitrogen lone pair on the inner ring of porphyrin, thus stabilizing $d_{x^2-y^2}$ orbitals. However, the binding between second pyridine and Co sites will not influence either anti-bonding or bonding characters in the *z* direction, leading to an unaffected d_{z^2} orbital and thus a weak binding to the second pyridine.

In order to verify the binding ability of MMPF-11, soft X-ray L-edge absorption spectroscopy (soft XAS), a widely used technology in multi-topic coordination chemistry, has been applied.[24] Soft X-ray $L_{2,3}$ XAS spectra (*2p-3d*) are presented in Figure 3b for MMPF-11 and metallic Co standard at the Co $L_{2,3}$ edges. These two main peaks in the spectra arise from the spin orbit interaction of the *2p* core-shell, representing transitions from the $2p_{3/2,1/2}$ states; the total intensity of the peaks is proportional to the number of empty *3d* valence states. With the help from soft XAS at the Co L-edge and resolved crystal structure of MMPF-11, the Co^{3+} local square planar environment can be confirmed. CoN_4 is a more reasonable structure which enhances the binding activity. The coordinatively unsaturated Co^{III} centers with low spin state (S = 0) has been reported to exhibit a more favorable binding energy of intermediates due to coordination between empty Co $3d_{z^2}$ orbital and lone pair electrons of N(pyridyl) atom, leading a ~40 kcal mol^{-1} higher binding energy (Table S2).[25] Figure 3b shows the soft XAS of MMPF-11 obtained using the TEY-XAS (solid line) and FY-XAS (dashed line) techniques in the Co L-edge region. There is no obvious difference between the Co valence on surface (around 5 nm) and internal surface (around 100 nm), indicating a consistent reaction environment for catalysis.

The UV/Visible spectroscopic analysis was performed primarily on tracking the intermediate species that take part in the catalytic reaction cycle. Figure S22 showed UV/Vis absorption spectra of Co^{III} meso-Tetraphenylporphyrin (Co-TPP) in CH_2Cl_2 at room temperature. Co-TPP displayed a strong *Soret* absorbance at 410 nm, while there was no absorbance for 4-pyridinecarboxaldehyde at the same wavelength. After adding a certain amount of 4-pyridinecarboxaldehyde (here denoted as **P**), a new band appeared at 434 nm, which can be the corresponding intermediate peak of Co-TPP coordinated with **P**. This indicated that Co-metalated porphyrin units are capable of binding the reactant. To gain further insight into the electrophilicity on substrate, a mixture of Co-TPP and **P** in DMSO-d_6 causes a

shift of –CHO proton signal to a higher field, indicating the Co-TPP acts as an electron withdrawing group (Figure S23). However, Co-TPP has no effect on the chemical shift of benzaldehyde (Figure S24). A mesomeric effect can be used to explain the shielding observed here, in which the protons in –CHO group and the *meta* position are more strongly shielded than in the *ortho* and *para* positions (Figure S25). Conceptual density functional theory (CDFT) calculations revealed a lower electrophilicity index of C in aldehyde group from 0.180 in **P** alone to 0.097 after binding with Co-TPP, suggesting the increase of the electron density and shielding effect (Figure S26). Thereby, the increased electronic density of –CHO group can reduce the unfavorable entropy of activation. This greatly promotes the condensation of the 1,3-dicarbonyl compound with the aldehyde to afford an α,β-unsaturated carbonyl compound (substrate A, as mentioned in Figure 2a), which accounts for the significant drop in the reaction using benzaldehyde.

A substrate sorption test using a reported method[26] was utilized to study the guest interaction with those catalysts including MMPF-11 and ZIF-8, as shown in Figure S27 and S28. ^{1}H NMR analysis indicated that MMPF-11 still takes up the largest amount of **P** substrate even after being submersed in $CDCl_3$ for 12 h, as compared to ZIF-8 without opening Lewis site. This suggests a pre-concentration effect for catalysis through MMPF-11.

The variation of the distance between cofacial Co-porphyrins promoted us to investigate the catalytic performance of acyl-transfer reactions in which the catalytic activity has been related to the framework-topology of porphyrinic MOFs.[11a] To illustrate the catalytic capabilities of MMPF-11, the acyl-transfer reaction between N-acetylimidezole (NAI) and 4-pyridylcarbinol (4-PC) producing 4-acetoxymethylpyridines (4-AMP) was carried out in acetonitrile at 50 °C. Control experiments were conducted for homogeneous Co-TPP, MMPF-5, MMPF-3, MMPF-2 and a blank under the same conditions. As shown in Figure 3c, MMPF-11 demonstrated the most efficient catalytic activity for the acyl-transfer studied here. We then compared the Co–Co distances in the porphyrin pairs. Obviously, the distances in MMPF-5 (22 Å) and MMPF-3 (29 Å) are significantly larger than that in MMPF-11 (16 Å) and MMPF-2 (10 Å). The preconcentration effects can lead to the rate enhancement when NAI and 4-PC diffuse into the MMPF and bind to the Co site within porphyrin rings via coordination interactions. Due to its proper alignment of porphyrin linkers, only MMPF-11 should be able to bring N-acetylimidezole (NAI) and 4-pyridylcarbinol (4-PC) together, thus making it more energetically favorable for them to encounter each other and react (Figure S29).

Conclusion

In summary, we have illustrated a targeting strategy to enhance shape-selectivity catalysis within MOFs, as exemplified by constructing a series of MMPFs that have readily accessible metal sites and feature permit-required confined cavities. The constructed MMPFs showcased how the achievement from the exclusive formation of thermodynamically more stable product to the kinetic product can be steadily improved through rational structure design, which was supported by the systematic experimental and computational mechanistic studies to reveal the relationships between crystal structure and catalysis performances. Ongoing work in our laboratory includes employing this strategy toward new aspects of heterogeneous catalysis based on the host-guest chemistry.

Acknowledgements

The authors acknowledge the Robert A. Welch Foundation (B-0027) for financial support of this work. Part of the work was performed under the auspices of the DOE by Lawrence Livermore National Laboratory (LLNL) under contract DE-AC52-07NA27344. ChemMatCARS Sector 15 is supported by the National Science Foundation under grant number NSF/CHE-1834750. This research used resources of the Advanced Photon Source, a U.S. Department of Energy (DOE) Office of Science User Facility operated for the DOE Office of Science by Argonne National Laboratory under Contract No. DE-AC02-06CH11357. The authors also extended their sincere appreciation to Researchers Supporting Program project no (RSP2023R79) at King Saud University, Riyadh, Saudi Arabia for partial funding this work. (AN) Some of the authors (AAB, YSL) acknowledge financial support through the Hydrogen Storage Materials Advanced Research Consortium (HyMARC) of the U.S. Department of Energy (DOE), Office of Energy Efficiency and Renewable Energy, Fuel Cell Technologies Office under contracts DE-AC52-07NA2734. The authors also acknowledge the support by NSF for high-performance computing resources thought the grant CHE-1531468.

Conflict of Interest

The authors declare no conflict of interest.

Data Availability Statement

The data that support the findings of this study are available from the corresponding author upon reasonable request.

Keywords: Heterogeneous Catalysis · Kinetic Control · Metal-Organic Framework · Porphyrin · Shape-Selectivity

[1] S. M. Csicsery, *Zeolites* **1984**, *4*, 202–213.
[2] B. Smit, T. L. Maesen, *Nature* **2008**, *451*, 671–678.
[3] L. Hedstrom, *Enzyme Specificity and Selectivity in Encyclopedia of Life Sciences*, Wiley, Chichester, **2010**, pp. 1–8.
[4] "Zeolite Catalysts as Enzyme Mimics": N. Herron, *Biocatalysis and Biomimetics*, American Chemical Society, Washington, **1989**, chap. 11, pp. 141–154 (ACS Symposium Series, Vol. 392).

[5] a) Q. Huang, Q. Niu, X. F. Li, J. Liu, S. N. Sun, L. Z. Dong, S. L. Li, Y. P. Cai, Y. Q. Lan, *Sci. Adv.* **2022**, *8*, eadd5598; b) J. Liu, T. A. Goetjen, Q. Wang, J. G. Knapp, M. C. Wasson, Y. Yang, Z. H. Syed, M. Delferro, J. M. Notestein, O. K. Farha, J. T. Hupp, *Chem. Soc. Rev.* **2022**, *51*, 1045–1097; c) A. Bavykina, N. Kolobov, I. S. Khan, J. A. Bau, A. Ramirez, J. Gascon, *Chem. Rev.* **2020**, *120*, 8468–8535; d) X. Zhang, C. Yang, P. An, C. Cui, Y. Ma, H. Liu, H. Wang, X. Yan, G. Li, Z. Tang, *Sci. Adv.* **2022**, *8*, eadd5678; e) Y. Zhou, S. Liu, Y. Gu, G. H. Wen, J. Ma, J. L. Zuo, M. Ding, *J. Am. Chem. Soc.* **2021**, *143*, 14071–14076; f) Z. B. Fang, T. T. Liu, J. Liu, S. Jin, X. P. Wu, X. Q. Gong, K. Wang, Q. Yin, T. F. Liu, R. Cao, H. C. Zhou, *J. Am. Chem. Soc.* **2020**, *142*, 12515–12523; g) Y. Chen, P. Li, J. Zhou, C. T. Buru, L. Dordevic, P. Li, X. Zhang, M. M. Cetin, J. F. Stoddart, S. I. Stupp, M. R. Wasielewski, O. K. Farha, *J. Am. Chem. Soc.* **2020**, *142*, 1768–1773; h) Y. S. Wei, M. Zhang, R. Zou, Q. Xu, *Chem. Rev.* **2020**, *120*, 12089–12174.

[6] a) X. T. Liu, B. B. Qian, D. S. Zhang, M. H. Yu, Z. Chang, X. H. Bu, *Coord. Chem. Rev.* **2023**, *476*, 214921; b) G. A. Leith, C. R. Martin, J. M. Mayers, P. Kittikhunnatham, R. W. Larsen, N. B. Shustova, *Chem. Soc. Rev.* **2021**, *50*, 4382–4410.

[7] J. Lee, O. K. Farha, J. Roberts, K. A. Scheidt, S. T. Nguyen, J. T. Hupp, *Chem. Soc. Rev.* **2009**, *38*, 1450–1459.

[8] a) C. M. McGuirk, M. J. Katz, C. L. Stern, A. A. Sarjeant, J. T. Hupp, O. K. Farha, C. A. Mirkin, *J. Am. Chem. Soc.* **2015**, *137*, 919–925; b) A. Broto-Ribas, C. Vignatti, A. Jimenez-Almarza, J. Luis-Barrera, Z. Dolatkhah, F. Gándara, I. Imaz, R. Mas-Ballesté, J. Alemán, D. Maspoch, *Nano Res.* **2021**, *14*, 458–465; c) X. Zhang, Z. Zhang, J. Boissonnault, S. M. Cohen, *Chem. Commun.* **2016**, *52*, 8585–8588.

[9] B. Gole, A. K. Bar, A. Mallick, R. Banerjee, P. S. Mukherjee, *Chem. Commun.* **2013**, *49*, 7439–7441.

[10] W. Zhang, A. Nafady, C. Shan, L. Wojtas, Y. S. Chen, Q. Cheng, X. P. Zhang, S. Ma, *Angew. Chem. Int. Ed.* **2021**, *60*, 24312–24317.

[11] a) P. Deria, D. A. Gomez-Gualdron, I. Hod, R. Q. Snurr, J. T. Hupp, O. K. Farha, *J. Am. Chem. Soc.* **2016**, *138*, 14449–14457; b) B. An, Z. Li, Y. Song, J. Zhang, L. Zeng, C. Wang, W. Lin, *Nat. Catal.* **2019**, *2*, 709–717; c) P. Ji, T. Drake, A. Murakami, P. Oliveres, J. H. Skone, W. Lin, *J. Am. Chem. Soc.* **2018**, *140*, 10553–10561; d) J. Li, H. Huang, W. Xue, K. Sun, X. Song, C. Wu, L. Nie, Y. Li, C. Liu, Y. Pan, H.-L. Jiang, D. Mei, C. Zhong, *Nat. Catal.* **2021**, *4*, 719–729; e) D. M. Shakya, O. A. Ejegbavwo, T. Rajeshkumar, S. D. Senanayake, A. J. Brandt, S. Farzandh, N. Acharya, A. M. Ebrahim, A. I. Frenkel, N. Rui, G. L. Tate, J. R. Monnier, K. D. Vogiatzis, N. B. Shustova, D. A. Chen, *Angew. Chem. Int. Ed.* **2019**, *58*, 16533–16537; f) M. T. Huxley, A. Burgun, H. Ghodrati, C. J. Coghlan, A. Lemieux, N. R. Champness, D. M. Huang, C. J. Doonan, C. J. Sumby, *J. Am. Chem. Soc.* **2018**, *140*, 6416–6425; g) B. Abeykoon, T. Devic, J. M. Greneche, A. Fateeva, A. B. Sorokin, *Chem. Commun.* **2018**, *54*, 10308–10311; h) G. Zhou, B. Wang, R. Cao, *J. Am. Chem. Soc.* **2020**, *142*, 14848–14853.

[12] A. M. Shultz, O. K. Farha, J. T. Hupp, S. T. Nguyen, *J. Am. Chem. Soc.* **2009**, *131*, 4204–4205.

[13] I. Agirrezabal-Telleria, I. Luz, M. A. Ortuno, M. Oregui-Bengoechea, I. Gandarias, N. Lopez, M. A. Lail, M. Soukri, *Nat. Commun.* **2019**, *10*, 2076.

[14] X. S. Wang, M. Chrzanowski, C. Kim, W. Y. Gao, L. Wojtas, Y. S. Chen, X. Peter Zhang, S. Ma, *Chem. Commun.* **2012**, *48*, 7173–7175.

[15] L. Meng, Q. Cheng, C. Kim, W. Y. Gao, L. Wojtas, Y. S. Chen, M. J. Zaworotko, X. P. Zhang, S. Ma, *Angew. Chem. Int. Ed.* **2012**, *51*, 10082–10085.

[16] X. S. Wang, M. Chrzanowski, L. Wojtas, Y. S. Chen, S. Ma, *Chem. Eur. J.* **2013**, *19*, 3297–3301.

[17] a) C. Y. Lee, O. K. Farha, B. J. Hong, A. A. Sarjeant, S. T. Nguyen, J. T. Hupp, *J. Am. Chem. Soc.* **2011**, *133*, 15858–15861; b) B. J. Burnett, P. M. Barron, C. Hu, W. Choe, *J. Am. Chem. Soc.* **2011**, *133*, 9984–9987; c) X. Zhao, X. Bu, Q. G. Zhai, H. Tran, P. Feng, *J. Am. Chem. Soc.* **2015**, *137*, 1396–1399; d) N. C. Burtch, K. S. Walton, *Acc. Chem. Res.* **2015**, *48*, 2850–2857.

[18] Deposition Number 2151866 (for **MMPF-11**) contains the supplementary crystallographic data for this paper. These data are provided free of charge by the joint Cambridge Crystallographic Data Centre and Fachinformationszentrum Karlsruhe Access Structures service.

[19] S. Brunauer, P. H. Emmett, E. Teller, *J. Am. Chem. Soc.* **1938**, *60*, 309–319.

[20] F. Bossert, W. Vater, *Med. Res. Rev.* **1989**, *9*, 291–324.

[21] L. Shen, S. Cao, J. Wu, J. Zhang, H. Li, N. Liu, X. Qian, *Green Chem.* **2009**, *11*, 1414.

[22] a) A. R. Katritzky, D. L. Ostercamp, T. I. Yousaf, *Tetrahedron* **1986**, *42*, 5729–5738; b) V. G. Santos, M. N. Godoi, T. Regiani, F. H. Gama, M. B. Coelho, R. O. de Souza, M. N. Eberlin, S. J. Garden, *Chem. Eur. J.* **2014**, *20*, 12808–12816.

[23] Z. Lin, Z. M. Zhang, Y.-S. Chen, W. Lin, *Angew. Chem. Int. Ed.* **2016**, *55*, 13739–13743.

[24] a) Z. Yin, M. Kasrai, G. M. Bancroft, K. Fyfe, M. L. Colaianni, K. H. Tan, *Wear* **1997**, *202*, 192–201; b) A. Bianconi, R. Z. Bachrach, S. B. M. Hagstrom, S. A. Flodström, *Phys. Rev. B* **1979**, *19*, 2837–2843; c) M. L. Baker, M. W. Mara, J. J. Yan, K. O. Hodgson, B. Hedman, E. I. Solomon, *Coord. Chem. Rev.* **2017**, *345*, 182–208.

[25] a) Y. N. Gong, W. H. Zhong, Y. Li, Y. Z. Qiu, L. R. Zheng, J. Jiang, H. L. Jiang, *J. Am. Chem. Soc.* **2020**, *142*, 16723–16731; b) D. J. Xiao, M. I. Gonzalez, L. E. Darago, K. D. Vogiatzis, E. Haldoupis, L. Gagliardi, J. R. Long, *J. Am. Chem. Soc.* **2016**, *138*, 7161–7170.

[26] X. L. Yang, M. H. Xie, C. Zou, Y. He, B. Chen, M. O'Keeffe, C. D. Wu, *J. Am. Chem. Soc.* **2012**, *134*, 10638–10645.

Manuscript received: March 25, 2023
Accepted manuscript online: May 2, 2023
Version of record online: May 17, 2023